The Double Pulsar

Michael Kramer
University of Manchester
Jodrell Bank Observatory, UK

Abstract. A new era in fundamental physics began with the discovery of pulsars 1967, the discovery of the first binary pulsar in 1974 and the first millisecond pulsar in 1982. Ever since, pulsars have been used as precise cosmic clocks, taking us beyond the weak-field regime of the solar-system in the study of theories of gravity. Their contribution is crucial as no test can be considered to be complete without probing the strong-field realm of gravitational physics by finding and timing pulsars. This is particularly highlighted by the discovery of the first double pulsar system which was discovered by our team in 2003. The double pulsar is unique in that both neutron stars are detectable as radio pulsars. This, combined with significantly higher mean orbital velocities and accelerations when compared to other binary pulsars, suggested that the system would become the best available testbed for general relativity and alternative theories of gravity in the strong-field regime. Indeed, this has been achieved only three years after its discovery with four independent strong-field tests of GR, more than has been obtained for any other system. Use of the theory-independent mass ratio of the two stars makes these tests uniquely different from all preceding studies. Our results confirm the validity of GR at the 0.05% level, which is by far the best precision yet achieved for the strong-field regime. Remarkably, the transverse velocity of the systems center of mass is extremely small, a result which is important for future GR tests and evolutionary studies.

1 Introduction

Rarely had the formulation of a single theory changed our view of the Universe so dramatically as Einstein's theory of general relativity (GR). Immediately after its publication, scientists were considering ways of testing GR to experimentally verify the revolutionary different effects that were predicted as deviations from Newton's theory of gravity which had ruled supreme for about three hundred years. Already during World War I., British scientists were planning two expeditions to test GR by observing a predicted bending of light around the Sun during a total solar eclipse to be observed in 1919 in Brazil and Africa. The expeditions indeed took place, and Sir Arthur Eddington himself analysed photographic plates taken during the eclipse that showed the apparent displacement of stars when they were positioned behind the Sun. This bending of light near massive bodies confirmed one of Einstein's predictions and propelled him to immediate global stardom. Today, 85 years after these historic observations, physicists are still trying to put GR to the test.

To date the theory of general relativity has passed all observational tests with flying colours. Nevertheless, GR may indeed not be the last word in our understanding of gravitational physics, and it is important to experimentally confront the theory with new observations to explore different aspects and/or achieve higher precision. While some of the most stringent tests of GR are obtained by satellite experiments in the solar system, these solar-system experiments are all made in the weak-field gravitational regime. Tests of the strong-field limit, in particular involving the radiative aspects of GR, need also to be tested. For instance, it is possible to construct theories, which would pass all solar-system tests but would show deviations from GR in the strong-field limit (see e.g. [1]). Precision tests in the strong-field regime are best achieved by observing radio pulsars.

One of the toughest tests ever has recently become possible by the discovery of

two pulsars which are found to be in a close, slowly decaying orbit that will eventually lead to the destruction of these objects, predicted to happen in about 85 million years. This system is widely known simply as the *double pulsar*.

2   Pulsars

Pulsars are highly magnetised, rotating neutron stars which emit a narrow radio beam along the magnetic dipole axis. As the magnetic axis is inclined to the rotation axis, the pulsar acts like a cosmic light-house emitting a radio pulse that can be detected once per rotation period when the beam is directed toward Earth. For some very fast rotating pulsars, the so-called millisecond pulsars (see Sect. 5), the stability of the pulse period is similar to that achieved by the best terrestrial atomic clocks. Using these astrophysical clocks by accurately measuring the arrival times of their pulses, a wide range of experiments is possible. For most of these it is not necessarily important *how* the radio pulses are actually created. We will consider some of the basic pulsar properties below.

Pulsars are born in supernova explosions of massive stars. Created in the collapse of the stars' core, neutron stars are the most compact objects next to black holes. From timing measurements of binary pulsars (see Sect. 7), we determine the masses of pulsars to be typically around $1.35 \pm 0.04 M_\odot$[2] although this range has been expanded recently from $\sim 1.2 M_\odot$ to $2.1 M_\odot$. Modern calculations for different equations of state produce results for the size of a neutron star which are quite similar to the very first calculations by Oppenheimer & Volkov [3], i.e. a diameter of about 20 km. Such sizes are consistent with independent estimates derived from X-ray light-curves and luminosities of pulsars (e.g. [4]).

Pulsars emit electromagnetic radiation and, in particular, magnetic dipole radiation as they essentially represent rotating magnets. Assuming that this is the dominant process of loss in rotational energy and hence responsible for the observed increase in rotation period, P, described by $\dot{P}$, we can equate the corresponding energy output of the dipole to the loss rate in rotational energy. We obtain an estimate for the magnetic field strength at the pulsar (equatorial) surface from

$$B_S = 3.2 \times 10^{19} \sqrt{P\dot{P}} \text{ Gauss,} \qquad (1)$$

with P measured in s and $\dot{P}$ in s s^{-1}. Millisecond pulsars (see Section 5) have lower field strengths of the order of 10^8 to 10^{10} Gauss which appear to be a result of their evolutionary history. These magnetic fields are consistent with values derived from X-ray spectra of neutron stars where we observe cyclotron lines [5].

3   Pulsars as radio sources

The periodic beacon sent by the pulsar clock is usually rather weak, both because the pulsar is distant and the size of the actual emission region is small. Estimates range down to a few metres, resulting in brightness temperatures of up to 10^{37} K [6]. Such values require a coherent emission mechanism which, despite almost 40 years of intensive research, is still unidentified. However, we seem to have some basic understanding, in which the magnetised rotating neutron star induces an electric quadrupole field which is strong enough to pull out charges from the stellar surface (the electrical force exceeds the gravitational force by a factor of $\sim 10^{12}$!), surrounding the pulsar with dense plasma. The magnetic field forces the plasma to co-rotate with the pulsar like a rigid body. This co-rotating *magnetosphere* can only extend up to a distance where the co-rotation velocity reaches the speed of light[1]. This distance

---

[1]Strictly speaking, the Alfvén velocity will determine the co-rotational properties of the magnetosphere.

defines the so-called light cylinder which separates the magnetic field lines into two distinct groups, i.e. *open and closed field lines*. Closed field lines are those which close within the light cylinder, while open field lines would close outside. The plasma on the closed field lines is trapped and will co-rotate with the pulsar forever. In contrast, plasma on the open field lines can reach highly relativistic velocities and can leave the magnetosphere, creating the observed radio beam at a distance of a few tens to hundreds of km above the pulsar surface (see Fig. 1).
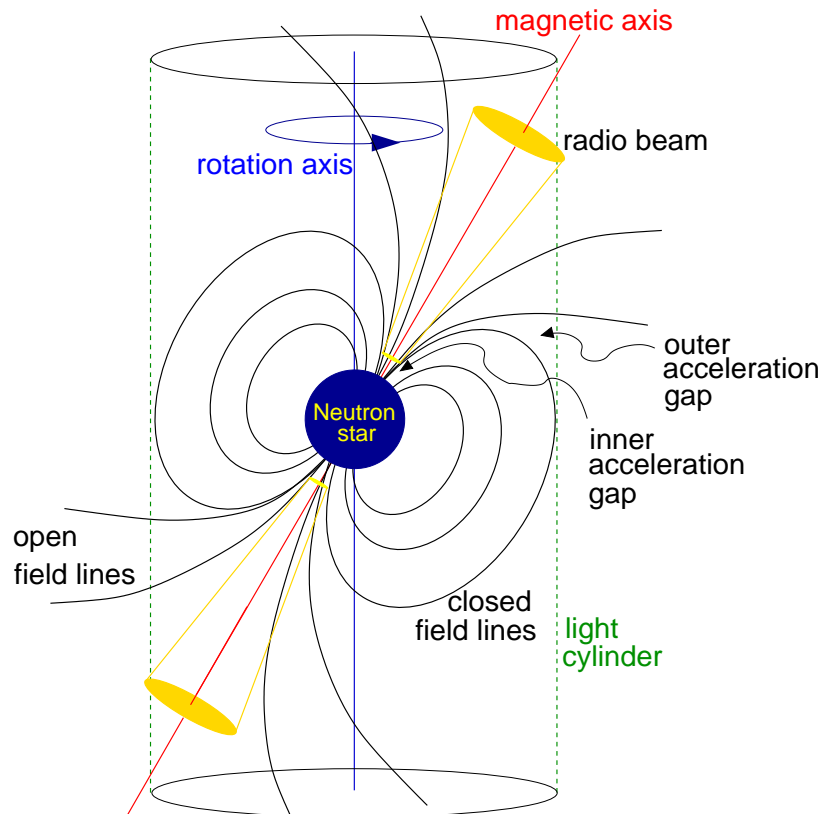

Figure 1: A pulsar is a rotating, highly magnetised neutron star. A radio beam centred on the magnetic axis is created in some distance to the pulsar. The tilt between the rotation and magnetic axes makes the pulsar in effect a cosmic lighthouse when the beam sweeps around in space.

Most pulsars are not strong enough to allow us a detection of their individual radio pulses, so that in most cases only an integrated pulse shape can be observed. If individual pulses are observable, they reflect the instantaneous plasma processes in the pulsar magnetosphere at the moment when the beam is directed towards Earth. The dynamics of these processes results in often seemingly random individual pulses, in particular when viewed with high time resolution. Despite this variety displayed by the single pulses, the mean pulse shape computed by averaging a few hundreds to few thousands of pulses is incredibly stable[7]. In contrast to the snapshot provided by the individual pulses, the average pulse shape, or *pulse profile*, can be considered as a long-exposure picture, revealing the global circumstances in the magnetosphere. These are mostly determined by geometrical factors and the strong magnetic field, leading to very stable pulse profiles. Apart from a distinct evolution with radio frequency, the same profiles are obtained, no matter where and when the pulses used to compute the average have been observed.

4   Evolution of Pulsars

As pulsars are powered by their rotational energy, their spin-frequency decreases with time. The slow-down can be described by

$$\dot{\nu} = -\text{const. } \nu^n \tag{2}$$

where the exponent, n, is known as the *braking index*. For magnetic dipole emission as the main energy loss, we expect $n = 3$. Measuring a second spin-frequency derivative, $\ddot{\nu}$, one can obviously determine the braking index via

$$n = \nu\ddot{\nu}/\dot{\nu}^2 \tag{3}$$

so that the assumption of dipole braking can be tested. However, this is only possible for the very youngest pulsars [8], whilst rotational instabilities known as *timing noise* can mimic a significant but time-varying value of $\ddot{\nu}$. These values then reflect timing noise rather than regular spin-down, so that derived braking indices are meaningless [9]. In total, only for five young pulsars could a braking index be determined that appears to reflect the long-term spin-down behaviour. With values ranging from $n = 1.4$ to $n = 2.9$ (e.g. [10]), the deviations from the expected braking index are not too severe.

Integrating Eqn. 2, we can estimate the age of a pulsar from

$$\tau = \frac{P}{(n-1)\dot{P}} = \frac{P}{2\dot{P}} = -\frac{\nu}{2\dot{\nu}} \tag{4}$$

where we have assumed a magnetic dipole braking index of $n = 3$. This quantity known as the *characteristic age* is a valid estimate for the true age under the assumption that the initial spin period is much smaller than the present period. While it had been assumed in the past that pulsars are born with periods similar to that estimated for the Crab pulsar, $P_0 = 19$ ms [11], recent estimates suggest a wide range of initial spin periods from 14 ms up to 140 ms [12].

We can describe the evolution of a pulsar in period, P, and slow-down, $\dot{P}$, in a logarithmic P-$\dot{P}$-diagram as shown in Figure 2 where we plot all of the ~ 1700 known pulsars for which P and $\dot{P}$ have been measured. Since the estimates for both magnetic field (Eqn. 1) and characteristic age (Eqn. 4) depend only P and $\dot{P}$, we can draw lines of constant magnetic field and constant characteristic age. Accordingly, young pulsars should be located in the upper left area of Fig. 2. Pulsars are generally considered to be young if their characteristic age is less than 100 kyr. Specifically, pulsars with characteristic ages of less than 10 kyr appear in the cross-hatched area, whilst pulsars with ages between 10 and 100 kyr are located in the hatched area. The latter pulsars are often compared to the Vela pulsar if they match its *spin-down luminosity*, i.e. $\dot{E} > 10^{36}$ erg s^{-1}. The spin-down luminosity is simply given by the loss in rotational energy which can be measured from the observed period and period derivative,

$$\dot{E} = 4\pi^2 I \dot{P} P^{-3} \text{ erg s}^{-1} \tag{5}$$

where a neutron star moment of inertia of $I = 10^{45}$ g cm^2 is assumed. Obviously, $\dot{E}$ represents the maximum energy output available for spin-powered pulsars across the *whole* electromagnetic spectrum. A line of a constant, Vela-like $\dot{E} = 10^{36}$ erg s^{-1} is shown in Fig. 2 together with a line for $\dot{E} = 10^{33}$ erg s^{-1}.

When pulsars age, they move into the central part of the $P - \dot{P}$-diagram where they spend most of their lifetime. Consequently, most known pulsars have spin periods between 0.1 and 1.0 s with period derivatives of typically $\dot{P} = 10^{-15}$ s s^{-1}. Selection effects are only partly responsible for the limited number of pulsars known with very long periods, the longest known period being 8.5 s [13]. The dominant effect is due to the "death" of pulsars when their slow-down has reached a critical state. This state

seems to depend on a combination of P and $\dot{P}$ which can be represented in the $P - \dot{P}$-diagram as a *pulsar death-line*. To the right and below this line (see Figure 2) the electric potential above the polar cap may not be sufficient to produce the particle plasma that is responsible for the observed radio emission. While this model can indeed explain the lack of pulsars beyond the death-line, the truth may be more complicated as the position of the 8.5-sec pulsar deep in the *pulsar graveyard* indicates. Nevertheless, it is clear that the normal life of radio pulsars is limited and that they die eventually after tens to a hundred million years. The position of a sub-set of about 100 pulsars located in the lower left part of Fig. 2 cannot be explained by the above picture of normal pulsar life. The evolution of these "millisecond pulsars" is different.

5   Formation of Millisecond Pulsars

The millisecond pulsars located in lower-left part of the $P - \dot{P}$ diagram are clearly different from the majority of pulsars. Firstly, they exhibit much shorter pulse periods. The first discovered millisecond pulsar, PSR B1937+21 [14], has has a period of only 1.56 ms and remained the pulsar with the shortest period known for more than 20 years. Only recently, a millisecond pulsar, PSR J1748-2446ad, was discovered which has a slightly shoter period of 1.40 ms [15]. Secondly, millisecond pulsars also have very small period derivatives, $\dot{P} \lesssim 10^{-18}$ s s^{-1}, making them much older (see Eqn. 4) than normal pulsars with ages up to $\sim 10^{10}$ yr. In the standard scenario, which finds its ultimate confirmation in the discovery of the double pulsar, millisecond pulsars are recycled from a dead binary pulsar via an X-ray binary accretion phase. The pulsars' millisecond periods are obtained when mass and thereby angular momentum is transferred from an evolving binary companion while it overflows its Roche lobe (e.g. [16]).

Even though most ordinary stars are in binary systems, most pulsars do not evolve into a millisecond pulsar. The birth of the pulsar usually disrupts the system, preventing the access to a mass donor and explaining why most pulsars are isolated. In the binary systems that survive the supernova explosion, the pulsar will eventually cease to emit radio emission, before the system evolves into a X-ray binary phase during which mass accretion onto the pulsar occurs. The pulsar spins up and is recycled into a radio millisecond pulsar when P and $\dot{P}$ have been altered such that the pulsar has crossed the death-line again in the other direction. The final spin period of such a recycled pulsar depends on the mass of the binary companion. A more massive companion evolves faster, limiting the duration of the accretion process and hence the angular momentum transfer.

The majority of millisecond pulsars will have had a low-massive companion. These systems evolve into low-mass X-ray binaries (LMXBs) and will result into a fast-spinning millisecond pulsar with period of $P \sim 1 - 10$ms with a low-mass white-dwarf companion. Systems with a more massive companion evolve into high-mass X-ray binaries (HMXBs) which represent the progenitors for double neutron star systems (DNSs). DNSs are rare since these systems need to survive a total of two supernova explosions. If this happens, the millisecond pulsar is only mildly recycled with a period of tens of millisecond.

The properties of millisecond pulsars and X-ray binaries are consistent with the described picture. For instance, it is striking that $\sim 80\%$ of all millisecond pulsars are in a binary orbit while this is true for only less than 1% of the non-recycled population. For millisecond pulsars with a low-mass white dwarf companion the orbit is nearly circular due to a circularisation of the orbit during the recycling process. In case of DNS systems, the orbit is affected by the unpredictable nature of the kick imparted onto the newly born neutron star in the asymmetric supernova explosion of the companion. If the system survives, the result is typically an eccentric orbit with an orbital period of a few hours.
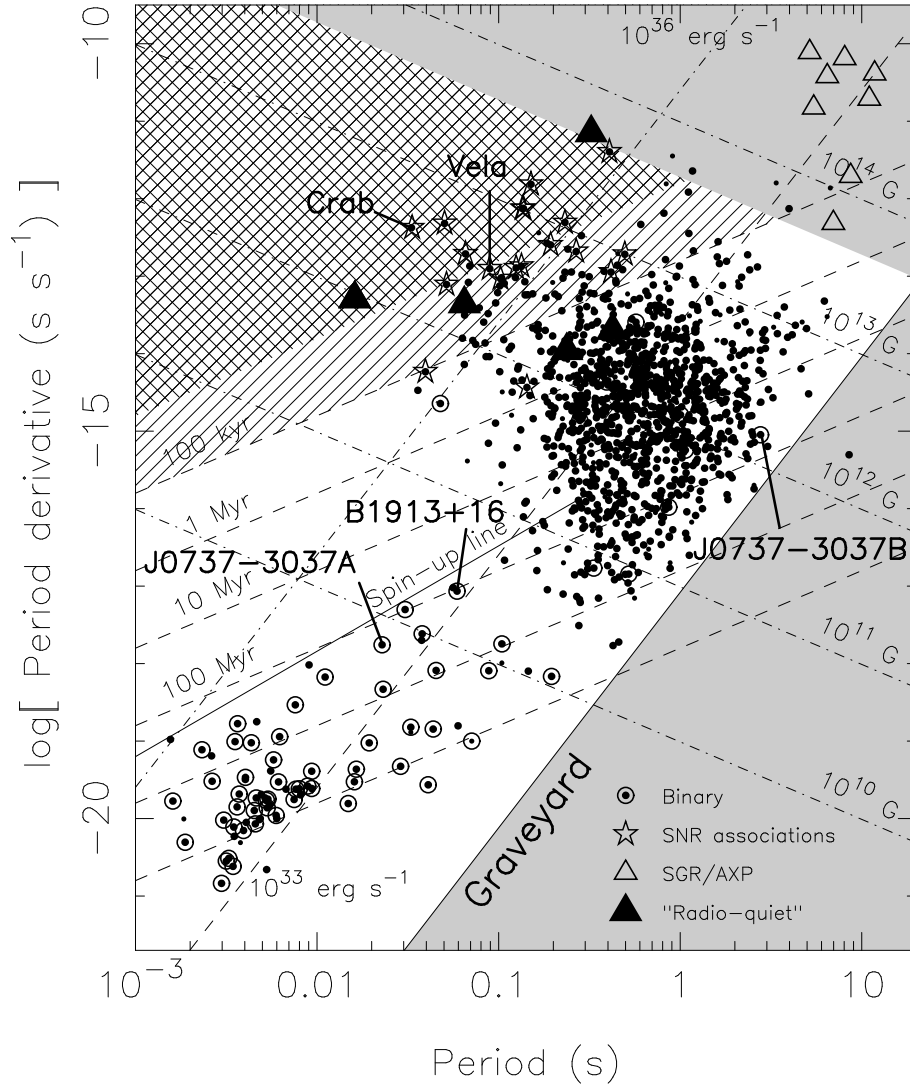
Figure 2: The $P - \dot{P}$–diagram for the known pulsar population. Lines of constant characteristic age, surface magnetic field and spin-down luminosity are shown. Binary pulsars are marked by a circle. The lower solid line represents the pulsar "death line" enclosing the "pulsar graveyard" where pulsars are expected to switch off radio emission. The grey area in the top right corner indicates the region where the surface magnetic field appears to exceed the quantum critical field of 4.4×10^{13} Gauss. For such values, some theories expect the quenching of radio emission in order to explain the radio-quiet "magnetars" (i.e. Soft-gamma ray repeaters, SGRs, and Anomalous X-ray pulsars, AXPs). The upper solid line is the "spin-up" line which is derived for the recycling process as the period limit for millisecond pulsars.

6   Pulsar Timing

The clock-like stability of pulsars means that through precise monitoring of pulsar rotations we can study a rich variety of phenomena that affect the propagation of their pulses. While the basic spin and astrometric parameters can be derived for essentially all pulsars, millisecond pulsars are the most useful objects for more exotic applications. Their pulse arrival times can be measured much more precisely than for normal pulsars (scaling essentially with the pulse period) and their rotation is also much smoother, making them intrinsically better clocks. Specifically, they usually do not exhibit rotational instabilities such as 'timing noise' and 'glitches' known for normal pulsars.

The key quantity of interest is the *time of arrival* (TOA) of pulses at the telescope. However, since individual pulses are usually too weak to be detected, and since they also show a jitter in arrival time within a window given by the extend of the pulse profile, it is the latter which is used for timing. The stability of pulse profiles allows us to compare the observed profile with a high signal-to-noise ratio template that is constructed from previous observations. The time-offset between template and profile determines the TOA. Because we use pulse profiles rather than individual pulses, the TOA is defined usually as the arrival time of the nearest pulse to the mid-point of the observation. As the pulses have a certain width, the TOA refers to some *fiducial point* on the profile. Ideally, this point coincides with the plane defined by the rotation and magnetic axes of the pulsar and the line of sight to the observer which is defined geometrically and independent of observing frequency or propagation effects.

The aim of pulsar timing is to count the number of neutron star rotations between two observations. Each TOA can therefore be assigned with a pulse number N which depends on rotation frequency ν and TOA t as

$$N = N_0 + \nu_0(t - t_0) + \frac{1}{2}\dot{\nu}(t - t_0)^2 + \frac{1}{6}\ddot{\nu}(t - t_0)^3 + \cdots \tag{6}$$

where N_0 is the pulse number at the reference epoch t_0. If t_0 coincides with the arrival of a pulse and the pulsar spin-down (i.e. ν and $\dot{\nu}$) is known accurately, the pulses should appear at integer values of N when observed in an inertial reference frame. However, our observing frame is not inertial: we are using telescopes that are located on a rotating Earth orbiting the Sun. Before analysing TOAs measured with the observatory clock (topocentric arrival times), we need to transfer them to the centre of mass of the Solar System (solar system barycentre, SSB). To a very good approximation, the SSB is an inertial reference frame.

The time transformation also corrects for any relativistic time delay that occurs due to the presence of masses in the Solar System. An additional advantage of analysing these barycentric arrival times is that they can easily be combined with other TOAs measured at different observatories at different times.

Given a minimal set of starting parameters, a least squares fit is needed to match the measured arrival times to pulse numbers according to Equation (6). We minimise the expression

$$\chi^2 = \sum_i \left(\frac{N(t_i) - n_i}{\sigma_i} \right)^2 \tag{7}$$

where n_i is the nearest integer to $N(t_i)$ and σ_i is the TOA uncertainty in units of pulse period (turns).

The aim is to obtain a phase-coherent solution that accounts for every single rotation of the pulsar between two observations. One starts off with a small set of TOAs that were obtained sufficiently close in time so that the accumulated uncertainties in the starting parameters do not exceed one pulse period. Gradually, the data set is expanded, maintaining coherence in phase. When successful, post-fit residuals expressed in pulse phase show a Gaussian distribution around zero with a root mean
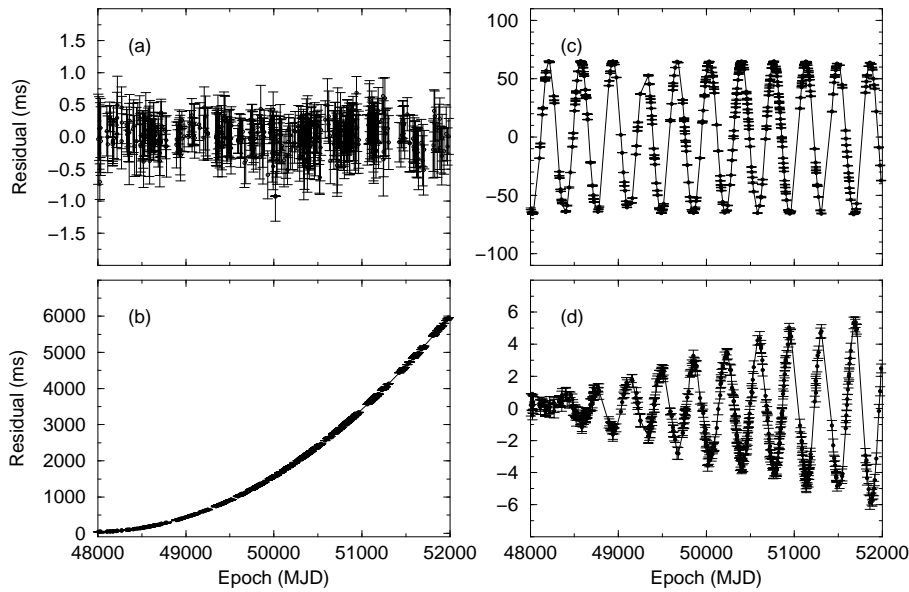
Figure 3: (a) Timing residuals for the 1.19 s pulsar B1133+16. A fit of a perfect timing model should result in randomly distributed residuals. (b) A parabolic increase in the residuals is obtained if $\dot{P}$ is underestimated, here by 4 per cent. (c) An offset in position (in this case a declination error of 1 arcmin) produces sinusoidal residuals with a period of 1 yr. (d) The effect of neglecting the pulsar's proper motion, in this case $\mu_{\mathrm{T}} = 380$ mas yr^{-1}. In all plots we have set the reference epoch for period and position to the first TOA at MJD 48000 to show the development of the amplitude of the various effects. Note the different scales on each of the vertical axes.

square that is comparable to the TOA uncertainties (see Fig. 3). A good test for the quality of the TOAs and their fit is provided by creating a new set of mean residuals, each formed by averaging n_{avg} consecutive post-fit residuals. The root mean square calculated from the new set should decrease with $\sqrt{n_{\mathrm{avg}}}$ if no systematics are present.

After starting with fits for only period and pulse reference phase over some hours and days, longer time spans slowly require fits for parameters like spin frequency derivative(s) and position. Incorrect or incomplete timing models cause systematic structures in the post-fit residuals identifying the parameter that needs to be included or adjusted (see Figure 3). The precision of the parameters improves with length of the data span and the frequency of observation, but also with orbital coverage in the case of binary pulsars.

7   Binary Pulsars

Observations of pulsars in binary orbits show a periodic variation in pulse arrival time. The timing model therefore needs to incorporate the additional motion of the pulsar as it orbits the common centre of mass of the binary system. For non-relativistic binary systems, the orbit can be described using Kepler's laws. For a number of binary systems however, the Keplerian description of the orbit is not sufficient and relativistic corrections need to be applied.

Kepler's laws can be used to describe a binary system in terms of the five Keplerian parameters, shown schematically in Figure 4. These five parameters are required to refer the TOAs to the binary barycentre: (a) orbital period, P_{b}; (b) projected semi-major orbital axis, $a_{\mathrm{p}} \sin i$ (see below); (c) orbital eccentricity, e; (d) longitude of periastron, ω; (e) the epoch of periastron passage, T_0.
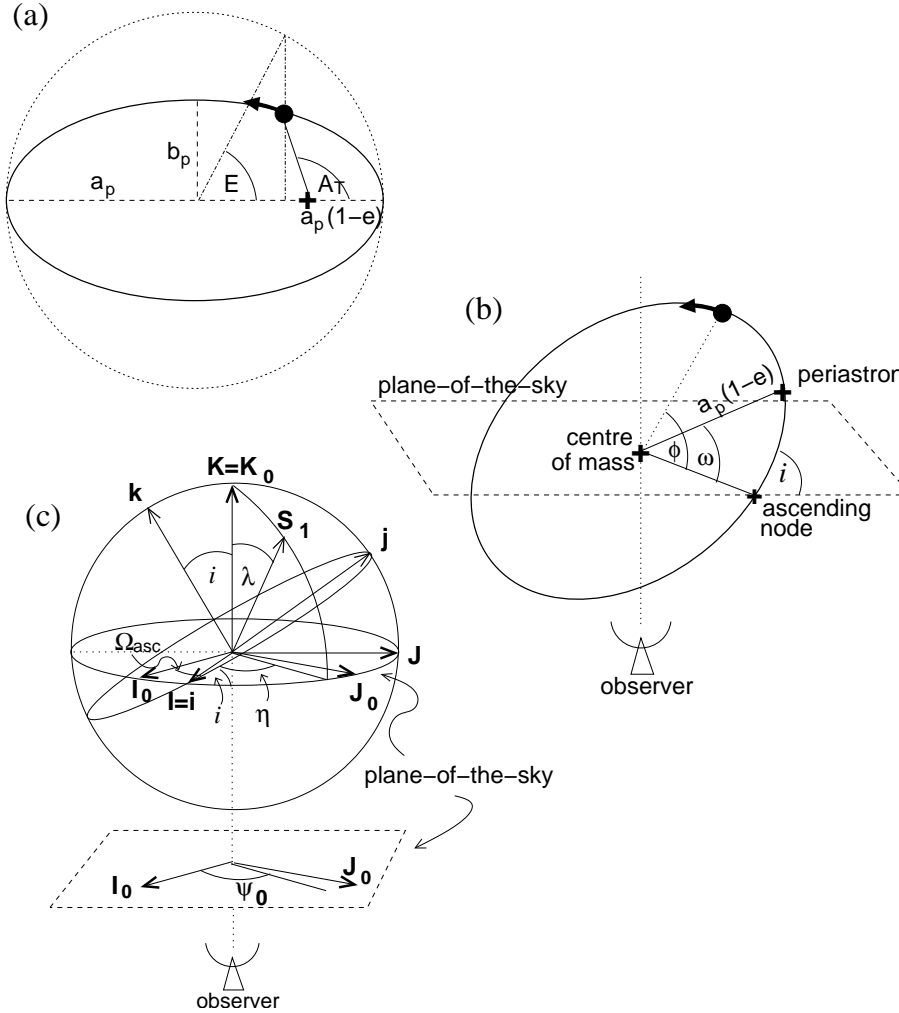
Figure 4: Definition of the orbital elements in a Keplerian orbit and the angles relating both the orbit and the pulsar to the observer's coordinate system and line of sight. (a) is drawn in the plane of the orbit; (b) shows the orbit inclined to the plane of the sky. The closest approach of the pulsar to the centre of mass of the binary system marks periastron, given by the longitude ω and a chosen epoch T_0 of its passage. The distance between centre of mass and periastron is given by $a_\mathrm{p}(1-e)$ where a_p is the semi-major axis of the orbital ellipse and e its eccentricity. (b) Usually, only the projection on the plane of the sky, $a_\mathrm{p} \sin i$, is measurable, where i is the orbital inclination defined as the angle between the orbital plane and the plane of the sky. The *true anomaly*, A_T, and *eccentric anomaly*, E, are related to the *mean anomaly* by Kepler's law. The orbital phase of the pulsar Φ is measured relative to the ascending node. (c) The spatial orientation of the pulsar's spin-vector, $\mathbf{S_1}$, is given by the angles λ and η in the coordinate system shown as defined by Damour and Taylor (1992). The angle Ω_asc gives the longitude of ascending node in the plane of the sky.

For pulsars in close binary systems about white dwarfs, other neutron stars, or perhaps eventually black holes, relativistic effects due to strong gravitational fields and high orbital velocities produce observable signatures in the timing residuals. Even though GR appears to be the best description of the strong-field regime to date [17], alternative theories of gravity nevertheless should be considered and tested against it. A straightforward means of comparison is to parameterise the timing model in terms of the so-called 'post-Keplerian' (PK) parameters. For point masses with negligible spin contributions, the PK parameters in each theory should only be functions of the a priori unknown pulsar and companion mass, M_{p} and M_{c}, and the easily measurable Keplerian parameters [18]. With the two masses as the only free parameters, an observation of two PK parameters will already determine the masses uniquely in the framework of the given theory. The measurement of a third or more PK parameters then provides a consistency check for the assumed theory.

The PK parameters are measured as additional parameters in a theory independent timing model which describes the pulse arrival times in a phenomenological way, using the Keplerian and PK parameters. The best timing model for describing relativistic binary pulsars is the Damour-Deruelle (DD) timing model [19, 20]. Applying this model to TOA measurements, the PK parameters are determined. They take different forms in different theories of gravity. In general relativity, the five most important PK parameters are given by (e.g. [18]):

$$\dot{\omega} = 3T_{\odot}^{2/3} \left(\frac{P_{\mathrm{b}}}{2\pi}\right)^{-5/3} \frac{1}{1-e^2} (M_{\mathrm{p}} + M_{\mathrm{c}})^{2/3}, \qquad (8)$$

$$\gamma = T_{\odot}^{2/3} \left(\frac{P_{\mathrm{b}}}{2\pi}\right)^{1/3} e \frac{M_{\mathrm{c}}(M_{\mathrm{p}} + 2M_{\mathrm{c}})}{(M_{\mathrm{p}} + M_{\mathrm{c}})^{4/3}}, \qquad (9)$$

$$\dot{P}_{\mathrm{b}} = -\frac{192\pi}{5}T_{\odot}^{5/3} \left(\frac{P_{\mathrm{b}}}{2\pi}\right)^{-5/3} \frac{\left(1 + \frac{73}{24}e^2 + \frac{37}{96}e^4\right)}{(1-e^2)^{7/2}} \frac{M_{\mathrm{p}}M_{\mathrm{c}}}{(M_{\mathrm{p}} + M_{\mathrm{c}})^{1/3}}, \qquad (10)$$

$$r = T_{\odot}M_{\mathrm{c}}, \qquad (11)$$

$$s = T_{\odot}^{-1/3} \left(\frac{P_{\mathrm{b}}}{2\pi}\right)^{-2/3} x \frac{(M_{\mathrm{p}} + M_{\mathrm{c}})^{2/3}}{M_{\mathrm{c}}}, \qquad (12)$$

where the masses M_p and M_c of pulsar and companion, respectively, are expressed in solar masses $(M_{\odot})$. We define the constant $T_{\odot} = GM_{\odot}/c^3 = 4.925490947\mu$s where G denotes the Newtonian constant of gravity and c the speed of light. The first PK parameter, $\dot{\omega}$, is the easiest to measure and describes the relativistic advance of periastron. It provides an immediate measurement of the total mass of the system, $(M_{\mathrm{p}} + M_{\mathrm{c}})$. The parameter γ denotes the amplitude of delays in arrival times caused by the varying effects of the gravitational redshift and time dilation (second order Doppler) as the pulsar moves in its elliptical orbit at varying distances from the companion and with varying speeds. The decay of the orbit due to gravitational wave damping is expressed by the change in orbital period, $\dot{P}_{\mathrm{b}}$. The other two parameters, r and s, are related to the Shapiro delay caused by the gravitational field of the companion. These parameters are only measurable, depending on timing precision, if the orbit is seen nearly edge-on.

The PK parameters listed above are those which have been measured in binary systems to date. However, the list can be extended (see [18]) if the binary system is extreme enough. We expect the double pulsar to be such a system where never before measured PK parameters will be needed to describe the observations adequately (see Section 10).

8   The double pulsar – a magnificent laboratory

Our team discovered the 22.8-ms pulsar J0737−3039 in April 2003 [21] in an extension to the hugely successful Parkes Multi-beam survey [22]. It was soon found to be a member of the most extreme relativistic binary system ever discovered: its short orbital period ($P_{\rm b} = 2.4$ hrs) is combined with a remarkably high value of periastron advance ($\dot\omega = 16.9\,{\rm deg\,yr}^{-1}$, i.e. four times larger than for the Hulse-Taylor pulsar PSR B1913+16). This large precession of the orbit was measurable after only a few days of observations. The system parameters predict that the two members of the binary system will coalesce on a short time scale of only ~ 85 Myr. This boosts the hopes for detecting a merger of two neutron stars with first-generation ground-based gravitational wave detectors by a factor of 5 to 10 compared to previous estimates based on only the double neutron stars B1534+12 and B1913+16 [21, 23].

In October 2003, we detected radio pulses from the second neutron star [24]. The reason why signals from the 2.8-s pulsar companion (now called PSR J0737−3039B, hereafter "B") to the millisecond pulsar (now called PSR J0737−3039A, hereafter "A") had not been found earlier, became clear when it was realized that B was only bright for two short parts of the orbit. For the remainder of the orbit, the pulsar B is extremely weak and only detectable with the most sensitive equipment. The detection of a young companion B around an old millisecond pulsar A and their position in the $P - \dot P$-diagram (see Figure 2) confirms the evolution scenario proposed for recycled pulsars (see Section 5) and provides a truly unique testbed for relativistic gravity and also plasma physics.

8.1   A laboratory for plasma physics

The double pulsar is not only a superb test-bed for relativistic gravity, but it also provides an unprecedented opportunity to probe the workings of pulsars. The pulse emission from B is strongly modulated with orbital phase, most probably as a consequence of the penetration of the A's wind into B's magnetosphere. Figure 5 shows the pulse intensity for B as a function of pulse phase and orbital longitude for three radio frequencies. The first burst of strong emission, centred near orbital longitude 210 deg, covers about 13 min of the orbit, while the second burst, centred near longitude 280 deg, is shorter and last only for about 8 min. This pattern is stable over successive orbits and obviously frequency independent over the range probed. Deep integrations reveal other orbital phases, where B is visible but much weaker than during the two main burst periods. The figure also shows that not only does the pulse intensity change with orbital phase, but that the pulse shape changes as well. At the start of the first burst the pulse has a strong trailing component and a weaker leading component which dies out in the later phases of the burst. In the second burst, there are two components of more equal amplitude. This is the first time that profile changes are observed that clearly depend on orbital phase. Decoding this pattern as the orbit precesses due to relativistic effects and the system is viewed from different directions, offers a unique chance to probe the magnetosphere. Indeed, as discussed later, the "light-curve" of B is changing with time, probably due to the effects of geodetic precession.

It is important to note that by simply seeing B functioning as a radio pulsar, albeit with orbital phases of rather weak emission, confirms our ideas about the location of the origin of radio emission: The fact that B is still emitting, despite the loss of most of its magnetosphere due to A's wind, indicates that the fundamental processes producing radio emission are likely to occur close to the neutron star surface – in accordance with emission heights determined for normal radio pulsars (see Section 3).

The quenching or attenuation of B's radio emission for most of its orbit is only part of the interaction between A and B that is observed. For about 27 seconds of the
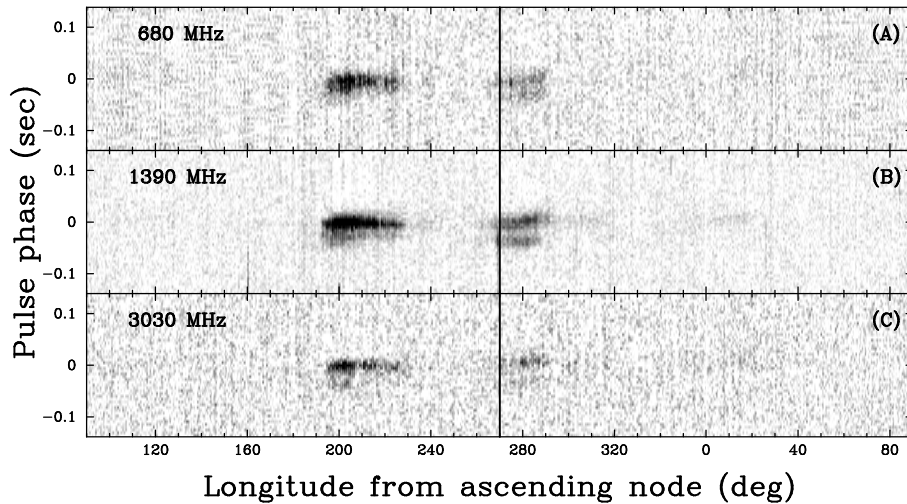
Figure 5: Grey-scale images showing the pulse of PSR J0737–3039B as a function of orbital phase at three observing frequencies (Lyne *et al.* 2004).

orbit, A's emission is eclipsed when A is lined up behind B at superior conjunction (Fig. 6). At that moment, the pulses of A pass in about 30,000km distance to the surface of B. It appears that the magnetospheric transmission for A's emission is modulated during the rotation of B, depending on the relative orientation of the spin-axis of B to A and our line-of-sight. Indeed, a modulation of the light-curve inside the eclipse region consistent with B's (full and half) rotation period is observed [25] (Fig. 7).

Perhaps even more exciting is the discovered evidence that A's radiation has some direct impact on the radiation pattern of B. Figure 8 shows a blow-up of B's emission at orbital phases where B is strongest. At the right orientation angles, a drifting sub-pulse pattern emerges that coincides with the arrival times of A's pulses at B [26]. This is the first time pulsar emission is observed to be triggered by some external force, and it is likely that this will help us to understand the conditions and on-set of pulsar emission in general.

8.2   A laboratory for strong-field gravity

Since neutron stars are very compact massive objects, the double pulsar (and other double neutron star systems) can be considered as almost ideal point sources for testing theories of gravity in the strong-gravitational-field limit. Timing observations of PSR J0737−3039A/B have been undertaken using the 64-m Parkes radio telescope in New South Wales, the 76-m Lovell radio telescope at Jodrell Bank Observatory, UK, and the 100-m Green Bank Telescope in West Virginia, between 2003 April and 2006 January. A total of 131,416 pulse times-of-arrival (TOAs) were measured for A while 507 TOAs were obtained for B using synthetic noise-free profile templates which are different for different frequency bands and, for B, functions of orbital phase and time. Pulsar and binary system parameters derived from these TOAs are listed in Table 1 at the end of this paper. Because of its narrower and more stable pulse profile, TOAs from A have a much higher precision than those from B and hence are used to determine the position, proper motion and main orbital parameters of the system. For B, the only fitted parameters were the pulse phase, the pulsar spin frequency, $\nu \equiv 1/P$, its first time-derivative $\dot{\nu}$ and the projected semi-major axis, $x_{\mathrm{B}} \equiv (a_{\mathrm{B}}/c)\sin i$.

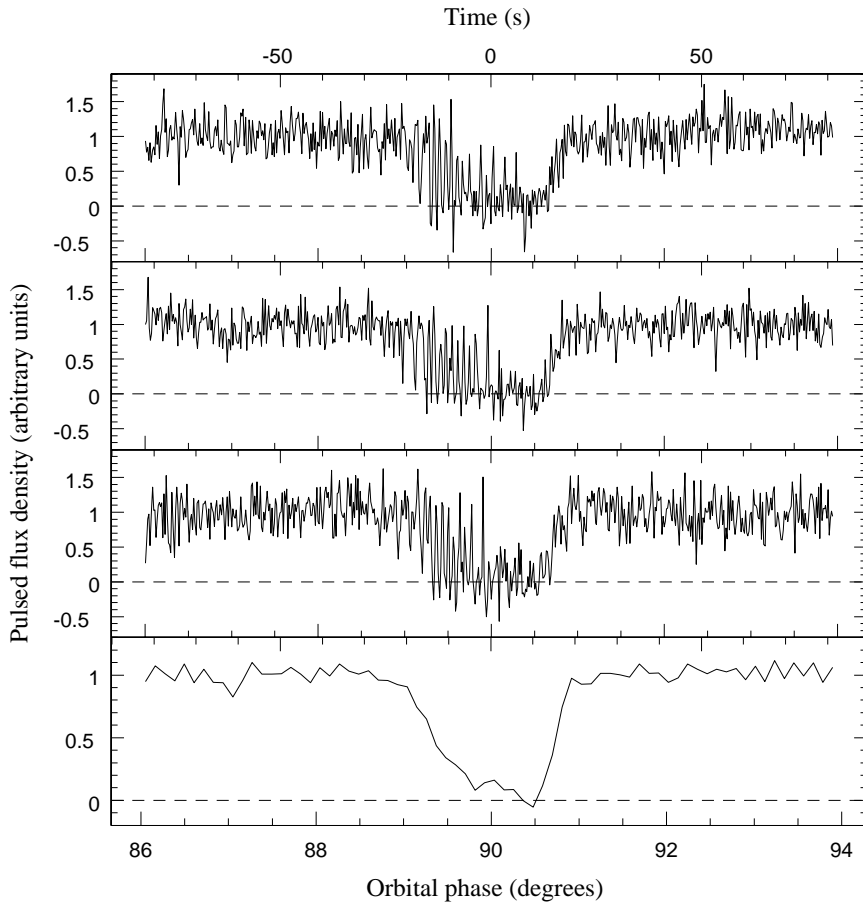Previous observations of PSR J0737−3039A/B[21, 24] resulted in the measure-

Figure 6: The pulsed flux density of A versus time (with respect to superior conjunction) and orbital phase for (top three panels) the three eclipses in the 820-MHz observation and (bottom panel) all three eclipses summed (McLaughlin et al. 2004b). In the individual eclipse light curves, every 12 pulses have been averaged for an effective time resolution of ~ 0.27 s. Every 100 pulses have been averaged to create the lower, composite light curve for an effective time resolution of ~ 2.3 s. Pulsed flux densities have been normalized such that the pre-eclipse average flux density is unity.

ment of R and four PK parameters: the rate of periastron advance $\dot{\omega}$, the gravitational redshift and time dilation parameter γ, and the Shapiro-delay parameters r and s. For the latest timing results [17] the measurement precision for these parameters has increased dramatically. Also, we have now measured the orbital decay, $\dot{P}_{\rm b}$, giving a total of five PK parameters for the system. Together with the mass ratio R, the measurements provide four independent tests of GR, more than for any other known system. The value of $\dot{P}_{\rm b}$, measured at the 1.4% level after only 2.5 years of timing, corresponds to a shrinkage of the orbit at a rate of 7mm per day. One can display these tests elegantly in a "mass-mass" diagram as shown in Figure 9. Measurement of the PK parameters gives curves on this diagram that are in general different for different theories of gravity but which should intersect in a single point, i.e., at a pair of mass values, if the theory is valid[18].

In addition to tests enabled by the PK parameters, the access to the orbit of both neutron stars – by timing A *and* B – provides yet another constraint on gravitational theories that is qualitatively different from what has been possible with previously known double neutron stars: using Kepler's third law, the measurement of
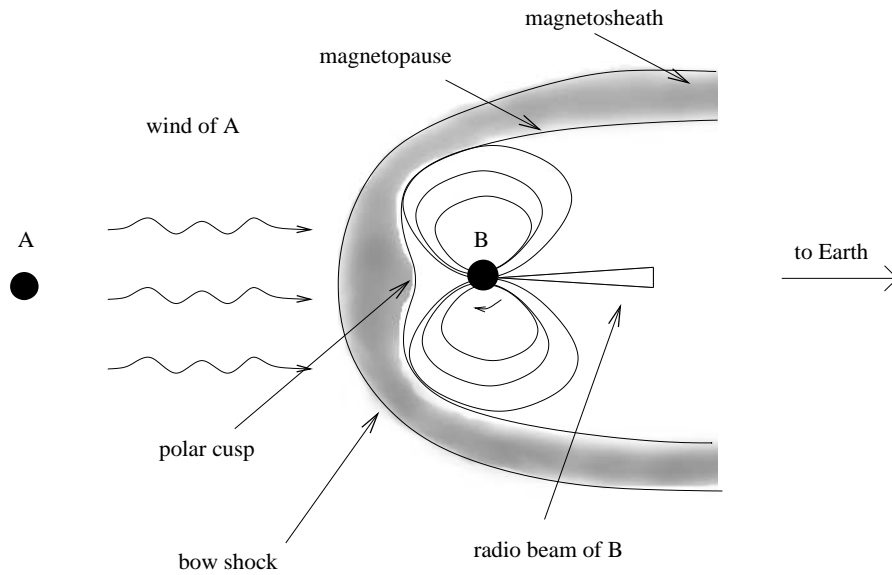
Figure 7: Cartoon (not to scale) showing the interaction between the relativistic wind of A and the magnetosphere of B when the radio beam of B is pointing towards the Earth (from McLaughlin et al. 2004b).
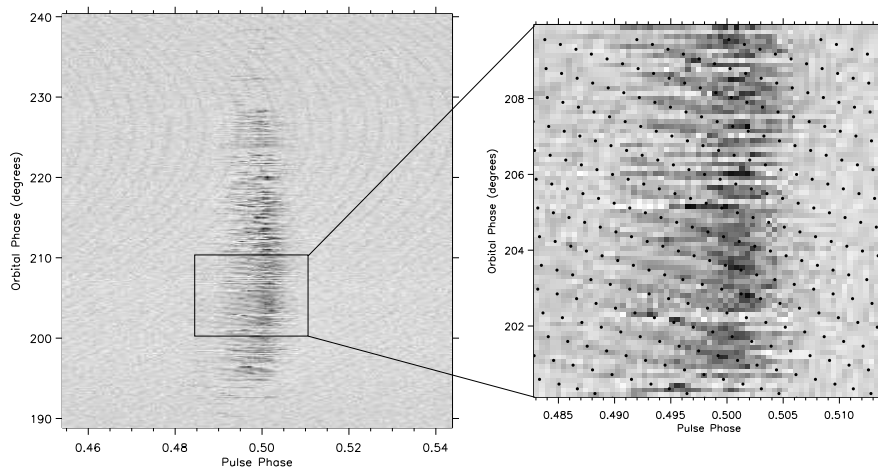

Figure 8: Observations of single pulses of B at 820 MHz for orbital phases 190 – 240 deg (only 10% of the pulse period is shown). Drifting features are present through most of these data, but are particularly obvious from orbital phases $\sim 200 - 210$deg which is enlarged on the right. Single pulses of A can be seen in the background of the left figure, where differential Doppler shifts from the orbital motion result in different apparent pulse periods and hence drifting patterns. The expanded view on the right is overlayed with dots marking the arrival of pulses of A at the centre of B, coinciding with the observed drift pattern in B. (McLaughlin et al. 2004a)

the projected semi-major axes of both orbits yields the mass ratio,

$$R(M_A, M_B) \equiv M_A/M_B = x_B/x_A. \tag{13}$$

For every realistic theory of gravity, we can expect R to follow this simple relation [18], at least to 1PN order. Most importantly, the R value is not only theory-independent, but also independent of strong-field (self-field) effects which is not the case for the PK parameters. In other words, any combination of masses derived from the PK parameters *must* be consistent with the mass ratio. The ability to measure this quantity provides therefore an important and unique constraint. With five PK parameters already available, this additional constraint also makes the double pulsar the most overdetermined system to date where the most relativistic effects can be studied in the strong-field limit.

Figure 9 shows that all measured constraints are consistent with GR. The most precisely measured PK parameter currently available is the precession of the longitude of periastron, $\dot{\omega}$. We can combine this with the theory-independent mass ratio R to derive the masses given by the intersection region of their curves: $m_A = 1.3381 \pm 0.0007\,\mathrm{M}_\odot$ and $m_B = 1.2489 \pm 0.0007\,\mathrm{M}_\odot$. Assuming GR and using these masses and the Keplerian parameters, we can predict values for the remaining PK parameters. Table 2 at the end of this paper lists results for the four independent tests that are currently available. The Shapiro delay (Figure 10) gives the most precise test, with $s_{\mathrm{obs}}/s_{\mathrm{pred}} = 0.99987 \pm 0.00050$. This is by far the best test of GR in the strong-field limit, having a higher precision than the test based on the observed orbit decay in the PSR B1913+16 system with a 30-year data span[30]. As for the PSR B1534+12 system[31], the PSR J0737$-$3039A/B Shapiro-delay test is complementary to that of B1913+16 since it is not based on predictions relating to emission of gravitational radiation from the system[32]. Most importantly, the four tests of GR presented here are qualitatively different from all previous tests because they include one constraint (R) that is independent of the assumed theory of gravity at the 1PN order. As a result, for any theory of gravity, the intersection point is expected to lie on the mass ratio line in Figure 9. GR also passes this additional constraint with the best precision so far.

8.2.1 A modification of the DD timing model

In order to study such possible effects and the performance of the standard timing software TEMPO[2] and its implementation of the DD timing model, we have made detailed simulations. Producing fake TOAs for a J0737$-$3039-like system, we varied the input parameter as $0.9 \leq s \leq 1.0$ and the assumed timing precision. For small TOA uncertainties, we can always recover the original s value by fitting the DD-model using TEMPO. However, comparing the standard TEMPO error estimates for s and r with estimates obtained from studying a corresponding χ^2 plane, the symmetric error bars given by TEMPO do not always correspond to the true uncertainties reflected by non-symmetric χ^2-contours if the TOA uncertainty is too large. This potential problem due to the non-linearity of the fitted parameters and correlations of the Shapiro delay parameters with the Römer delay in the orbit is well known. Hence, one usually explores an χ^2-plane evenly sampled in $\sqrt{1-s^2}$ and r to obtain reliable values and error estimates (see e.g. [34]). Increasing the TOA uncertainties, numerical fits to the fake TOAs assuming a $\sin i$ very close to unity (e.g. $\sin i = 0.99999$ or $i = 89.2$) sometimes results in fits with $s > 1$ due to numerical uncertainties. In order to remedy this situation we developed a modification of the DD timing model following a suggestion by Thibault Damour (priv. communication).

In the DD model, we fit for r and s which in GR becomes $s = \sin i$ where r is identical with the companion mass apart from a constant factor, $T_\odot$ (see Eqns. 11
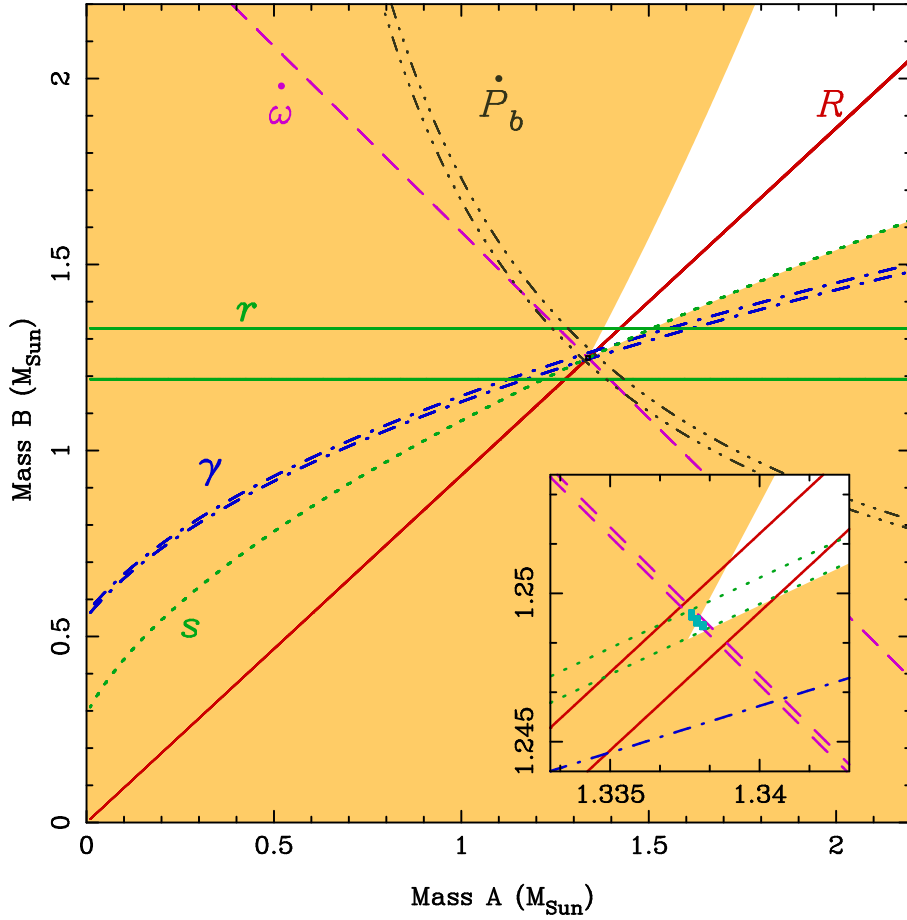
---

[2]http://pulsar.princeton.edu/tempo/

Figure 9: 'Mass–mass' diagram showing the observational constraints on the masses of the neutron stars in the double pulsar system J0737–3039 (Kramer et al. 2006). The shaded regions are those that are excluded by the Keplerian mass functions of the two pulsars. Further constraints are shown as pairs of lines enclosing permitted regions as given by the observed mass ratio and PK parameters as predicted by general relativity. Inset is an enlarged view of the small square encompassing the intersection of these constraints (see text).

and 12). In the new model, called DDS (for DD-Shapiro, see [35]), we write

$$s = 1 - e^{-z_s} \tag{14}$$

where z_s replaces s as our new fit parameter. It follows that

$$z_s = -\ln(1 - s). \tag{15}$$

The advantage becomes apparent when we compare this expression to the Shapiro delay term, Δ_s in the timing formula, in particular when comparing it to low-eccentricity pulsars for which (e.g. [36])

$$\Delta_s = -2r \ln(1 - s \sin \Phi) \tag{16}$$

where Φ is the orbital phase measured from the ascending node. At $\Phi = \pi/2$, the maximum delay is obtained

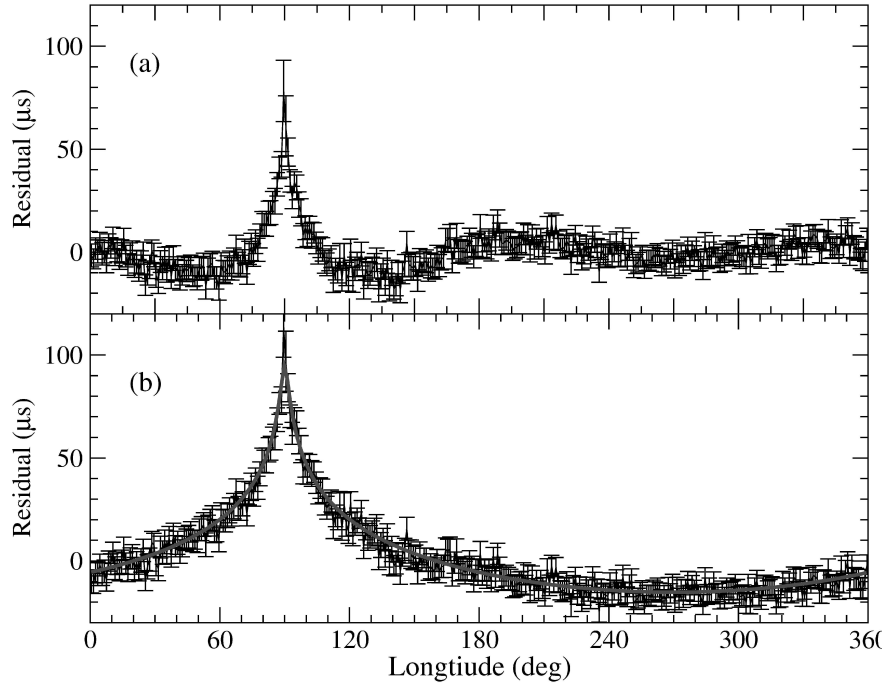$$\Delta_s^{max} = -2r \ln(1 - s) \tag{17}$$

Figure 10: The effect of the Shapiro delay caused by the gravitational potential of B seen in the timing residuals of A. (a) Observed timing residuals after a fit of all model parameters given in Table 1 *except* the Shapiro-delay terms r and s which were set to zero. (b) Residuals illustrating the full Shapiro delay, obtained by holding all parameters to their values given in Table 1, except the Shapiro delay terms which were set to zero. The line shows the predicted delay at the centre of the data span. In both cases, residuals were averaged in $1°$ bins of longitude (Kramer et al. 2006).

which has obvious similarities to our definition of z_s,

$$\Delta_s^{max} = 2\, r\, z_s \tag{18}$$

or

$$z_s = \Delta_s^{max}/2r. \tag{19}$$

Due to the nature of this simple transformation, a fit of the TOAs to the DD and DDS models always produces the same results. In addition, however, at large inclination angles the uncertainties on z_s derived by TEMPO are still consistent with those obtained from studies of corresponding χ^2 hyperspheres, often removing the need for the often computationally expensive calculation of the χ^2 plane. Using the DDS model, it is in particular impossible that numerical uncertainties lead to fit results which in GR correspond to values $\sin i > 1.0$. We are aware that the DDS model therefore represents a restriction of the parameter space which may be allowed by alternative theories of gravity.

The application of the DD and DDS model to the real TOAs produces consistent results and verifies the previous findings that s is significantly lower than the scintillation results which are consistent with our measurement only at the 3-σ level. Scintillation observations over the whole orbit have also been used to deduce the system transverse velocity. Ransom et al.[37] derive a value of 141 ± 8.5 km s^{-1} while Coles et al.[33] obtain 66 ± 15 km s^{-1} after considering the effect of anisotropy in the scattering screen. Both of these values are in stark contrast to the value of

10 ± 1 km s^{-1} (relative to the solar system barycentre) obtained from pulsar timing (Table 1). We note that the scintillation-based velocity depends on a number of assumptions about the properties of the effective scattering screen. In contrast, the proper motion measurement has a clear and unambiguous timing signature, although the transverse velocity itself scales with the pulsar distance. Even allowing that unmodeled effects of Earth motion could affect the published scintillation velocities by about 30 km s^{-1}, the dispersion-based distance would need to be underestimated by a factor of several to make the velocities consistent. We believe this is very unlikely, particularly as the tentative detection of a parallax gives us some confidence in the dispersion-based distance estimate. Hence, our timing results for both inclination angle and transverse velocity are less susceptible to systematic errors and are therefore more secure than those based on scintillation.

We have studied other effects possible affecting the timing results such as a possible variation of the dispersion measure as a function of orbital phase. However, the non-detection of any such effect leads us to the conclusion that in contrast unmodeled effects may have altered the scintillation results and the derived uncertainties on the inclination angle. An exciting explanation for the discrepancy may be that the emission of A suffers measurable refraction while propagating through the magnetosphere of B. If that were indeed the case, we would have a direct handle onto the magneto-ionic properties of B's magnetosphere for the first time, e.g. corresponding plasma densities in B's magnetosphere would need to be relatively large.
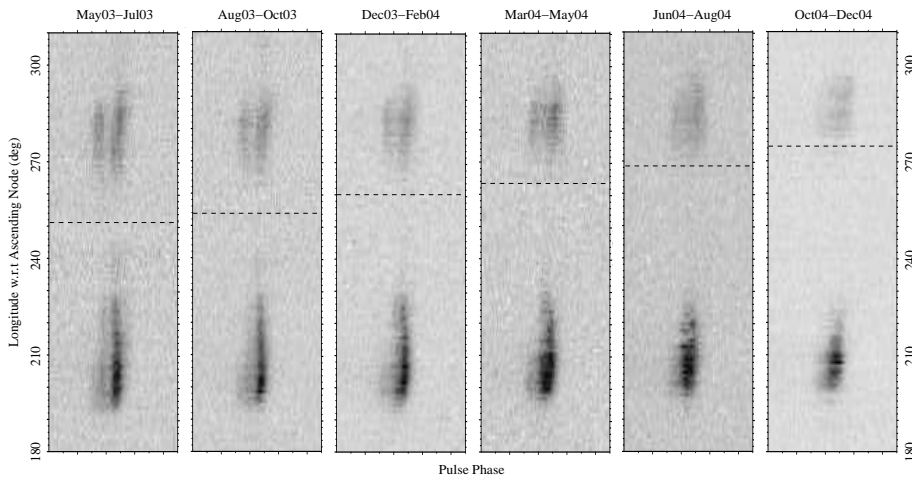

Figure 11: The emission of B at 1390 MHz as a function of the orbital longitude (vertical axis) and for the pulse phase range 0.18–0.27 (horizontal axis) as in Figure 5. Each panel was obtained by adding all the data in the ~ 3 months period indicated at the top of each panel. The dashed lines represent the position of the periastron at the given epoch. A change in the visibility pattern of B is clearly visible and most likely caused by geodetic precession (Burgay et al. 2005).

The short eclipses in A's emission already indicate that we are observing the system almost completely edge-on. This is confirmed independently by measuring a Shapiro delay and inferring (in GR) that the inclination angle i is indeed close to $90°$. Other methods using the variation of the pulsars's intensity due the turbulent interstellar medium are available for an independent measurement of the orbital orientation. Based on such scintillation observations of both pulsars over the short time interval when A is close to superior conjunction, Coles et al.[33] derived a value the orbital inclination angle i that is very close to $90°$, i.e. they derive $|i - 90°| = 0°.29 \pm 0°.14$. In GR, the parameter s can be identified with $\sin i$ where i is the inclination angle of the orbit. The value of s derived from our timing observations (Table 1) corresponds

to $i = 88°.69^{+0°.50}_{-0°.76}$. Comparing the two methods, one notes that the scintillation results are based on correlating the scintillation properties of A and B over the short time-span of the orbital motion when they are in conjunction to the observer. In contrast, the measurement of the inclination angle from timing measurements results from detecting significant harmonic structure in the post-fit residuals after parts of the Shapiro delay are absorbed in the fit for the Römer delay, i.e. the light travel time across the orbit. As shown in Figure 10, these structures are present throughout the whole orbit, so that the results from timing measurements may be expected to be more reliable. However, as all TOAs are associated with uncertainties, we need to make sure that a multi-parameter least-square fit of the DD model will reproduce the correct value of the PK parameters s and r despite possible numerical effects.
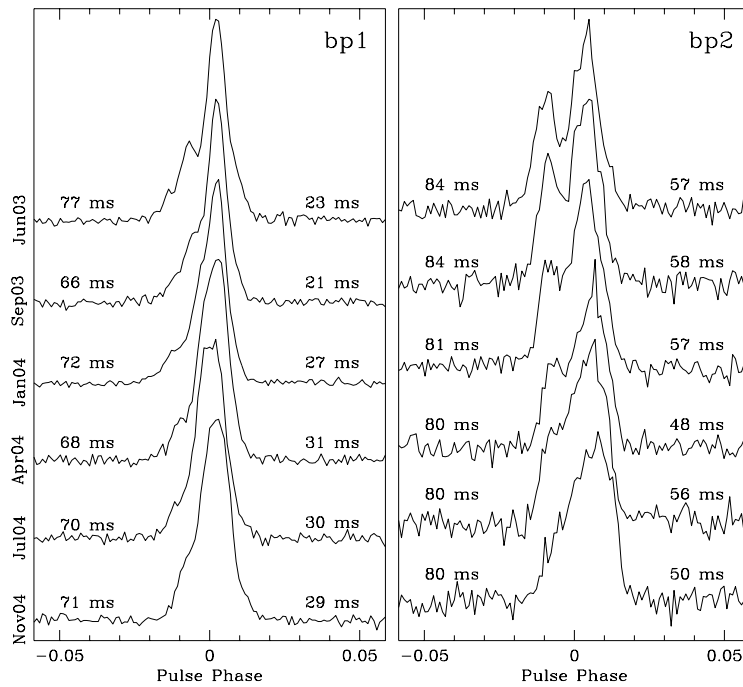

Figure 12: Pulse shapes of B in the two bright phases (see previous figure) as a function of time, again in in three month intervals. Again, a systematic change in the pulse profile is clearly visible. (Burgay et al. 2005).

8.2.2   Effects of geodetic precession

The measurement of the times-of-arrival (TOAs) are obtained with a standard "template matching" procedure that involves a cross-correlation of the observed pulse profile with high signal-to-noise ratio template (e.g. [38]). Any change in the pulse profile could lead to systematic variations in the measured TOAs. We performed detailed studies of the profiles of A and B to investigate any possible profile changes with time as such as expected from another effect predicted by GR.

In GR, the proper reference frame of a freely falling object suffers a precession with respect to a distant observer, called geodetic precession. In a binary pulsar system this geodetic precession leads to a relativistic spin-orbit coupling, analogous to spin-orbit coupling in atomic physics [39]. As a consequence, both pulsar spins precess about the total angular momentum, changing the relative orientation of the pulsars to one another and toward Earth. Since the orbital angular momentum is much larger than the pulsars' angular momenta, the total angular momentum is effectively
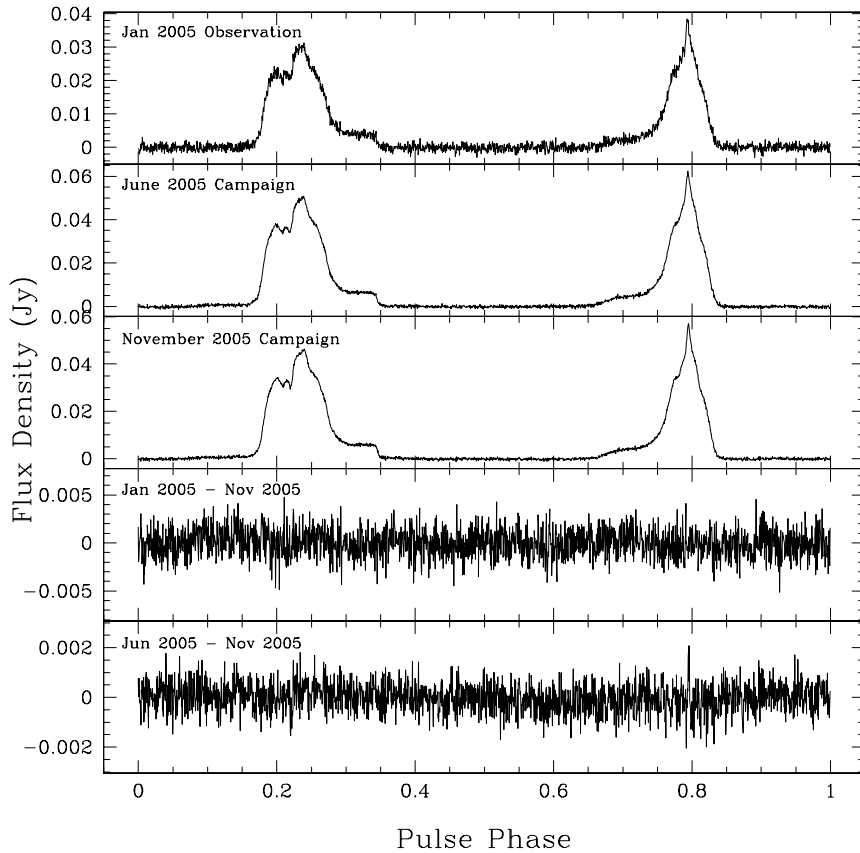
Figure 13: Pulse profiles of A observed at three different epochs. Subtracting one profile from the others does not reveal any significant changes as demonstrated in the two bottom plots. Figure provided by Rob Ferdman & Ingrid Stairs.

represented by the orbital angular momentum. The precession rate [40] depends on the period and the eccentricity of the orbit as well as the masses of A and B. With the orbital parameters of the double pulsar, GR predicts precession periods of only 75 yr for A and 71 yr for B.

Geodetic precession has a direct effect on the timing as it causes the polar angles of the spins and hence the effects of aberration to change with time [18]. These changes modify the *observed* orbital parameters, like projected semi-major axis and eccentricity, which differ from the *intrinsic* values by an aberration dependent term, potentially allowing us to infer the system geometry (see Section 10). Extracting the signature of these effects in the timing data is a goal for the years to come. Other consequences of geodetic precession can be expected to be detected much sooner and are directly relevant for the timing of A and B. These arise from variations in the pulse shape due to changing cuts through the emission beam as the pulsar spin axes precess. Moreover, geodetic precession also leads to a change in the relative alignment of the pulsar magnetospheres, so that the visibility pattern and even the profile of B should vary due to these changes as well.

Indeed, studies of the profile evolution of B [41] reveal a clear evolution of B's emission on orbital and secular time-scales. The light-curves of B (i.e. the visibility of B versus orbital phase) undergo clear changes (Figure 11) while the profile of B as observed in the bright orbital phases is clearly changing with time also (Figure 12).

These phenomena are probably caused by a changing magnetospheric interaction due to geometry variations resulting from geodetic precession. In any case, these changes require sophisticated timing analysis techniques.

For the timing of B, because of the orbital and secular dependence of its pulse profile, different templates were used for different orbital phases and different epochs. A matrix of B templates was constructed, dividing the data set into 3-month intervals in epoch and 5-minute intervals in orbital phase. The results for the 29 orbital phase bins were studied, and it was noticed that, while the profile changes dramatically and quickly during the two prominent bright phases, the profile shape is simpler and more stable at orbital phases when the pulsar is weak. In the final timing analysis for pulsar B, we therefore omitted data from the two very bright orbital phases. We also used an unweighted fit to avoid biasing the fit toward remaining brighter orbital phases.

Since the overall precision of our tests of GR is currently limited by our ability to measure x_B and hence the mass ratio $R \equiv m_A/m_B = x_B/x_A$, we adopted the following strategy to obtain the best possible accuracy for this parameter. We used the whole TOA data set for B in order to measure B's spin parameters P and $\dot{P}$, given in Table 1 of the main paper. These parameters were then kept fixed for a separate analysis of two concentrated 5-day observing sessions. On the timescale of the long-term profile evolution of B, each 5-day session represents a single-epoch experiment and hence requires only two sets of profile templates. The value of x_B obtained from a fit of this parameter only to the two 5-day sessions is presented in Table 1 of the main paper.

The study of the profile evolution of A [42, 17] did not lead to the detection of any profile change (see Figure 13). This present non-detection greatly simplifies the timing of A but does not exclude the possibility that changes may happen in the future. While the effects of geodetic precession could be small due to a near alignment of pulsar A's spin and the orbital momentum vector, the results could also be explained by observing the system at a particular precession phase. While this case appears to be relatively unlikely, it must not be excluded as such a situation had indeed occurred for PSR B1913+16 [43]. Indeed, a modelling of the results suggests that this present non-detection of profile changes is consistent with a rather wide range of possible system geometries. One conclusion that can be drawn is that the observations are inconsistent with the large profile changes that had been predicted by some models [44]. Fortunately, independent information is available that suggests that the alignment angle, and hence the impact of geodetic precession, may indeed be very small. This information is derived from a study of the evolution of the system based on the rather small transverse velocity of the double pulsar.

8.3   Space-motion and evolution of the double pulsar

The timing results indicate that the space velocity of the double pulsar system is surprisingly small. Based on the measured dispersion measure and a model for the Galactic electron distribution[29], PSR J0737−3039A/B is estimated to be about 500 pc from the Earth. From the timing data we have measured a marginally significant value for the annual parallax, 3 ± 2 mas, corresponding to a distance of $200 - 1000$ pc (Table 1), which is consistent with the dispersion-based distance that was also used for studies of detection rates in gravitational wave detectors [21]. The observed proper motion of the system (Table 1) then implies a transverse space velocity of only 10 km s^{-1} with a velocity vector parallel to the Galactic plane. With this information, Stairs et al. (2006) [45] examined the history and formation of this system, determining estimates of the pre-supernova companion mass, orbital separation, supernova kick and misalignment angle between the pre- and post-supernova orbital planes. One of the surprising results is that the progenitor to the recently formed B was probably less than $2\,M_\odot$, lending credence to suggestions that this object may not have formed in a normal core-collapse supernova. They conclude that it therefore must be possible,

in at least some cases, for low-mass helium stars to undergo Supernova explosions, and that there must be a range of progenitor types that can produce double neutron star systems. The relative frequency of the different types must depend on the initial mass function and ranges of binary orbits. This will have implications for the number of double neutron systems in the Galaxy, the retention of neutron stars in globular clusters and for the apparent dearth of isolated mildly recycled pulsars ejected from unbinding second SN explosions.

The study of the double pulsar evolution [45] also suggests that the kick velocity was rather small and that the misalignment angle between the spin of pulsar A and the total angular momentum vector (after the second supernova explosion) is probably much less than $10°$. In this case, the expected impact of geodetic precession on pulsar A's profile is rather small, consistent with the present observational evidence. This makes us confident that high-precision timing observations of A will continue for quite a while (in contrast to, for instance, the Hulse-Taylor pulsar which may disappear as a radio source at about 2025 [43]). At the same time, the small velocity of the double pulsar system is also extremely good news for tests of alternative theories of gravity where the measurement of the orbital decay is extremely useful.

9   Orbital decay measurement & Alternative theories of gravity

Because the measured uncertainty in $\dot{P}_{\rm b}$ decreases approximately as $T^{-2.5}$, where T is the data span, we expect to improve our test of the radiative aspect of the system to the 0.1% level or better in about five years' time. For the PSR B1913+16 and PSR B1534+12 systems, the precision of the GR test based on the orbit-decay rate is severely limited both by the uncertainty in the differential acceleration of the Sun and the binary system in the Galactic gravitational potential and the uncertainty in pulsar distance[46, 31]. For PSR J0737−3039A/B, both of these corrections are very much smaller than for these other systems. Based on the measured dispersion measure and a model for the Galactic electron distribution[29], PSR J0737−3039A/B is estimated to be about 500 pc from the Earth. From the timing data we have measured a marginally significant value for the annual parallax, 3±2 mas, corresponding to a distance of 200−1000 pc (Table 1), which is consistent with the dispersion-based distance that was also used for studies of detection rates in gravitational wave detectors [21]. The observed proper motion of the system (Table 1) and differential acceleration in the Galactic potential [47] then imply a kinematic correction to $\dot{P}_{\rm b}$ at the 0.02% level or less. Independent distance estimates also can be expected from measurements of the annual parallax by Very Long Baseline Interferometry (VLBI) observations, allowing a secure compensation for this already small effect. A measurement of $\dot{P}_{\rm b}$ at the 0.02% level or better will provide stringent tests for alternative theories of gravity as many are, for instance, predicting a significant amount of gravitational *dipole* radiation. Hence, a confirmation that the observations of the double pulsar are consistent with emission of gravitational *quadrupole* radiation to a very high level ofprecisionn promises to put limits on some scalar-tensor theories that will surpass even the best current Solar-system tests [48].

10   Future tests

In estimating the future improvements in the uncertainty of $x_{\rm B}$, and hence R and our current precision for GR tests, we need to consider that geodetic precession will lead to changes to the system geometry and hence to the aberration of the rotating pulsar beam. The effects of aberration on pulsar timing are usually not separately measurable but are absorbed into a redefinition of the Keplerian parameters. As a result, the observed projected sizes of the semi-major axes, $x_{\rm A,B}^{\rm obs}$, differ from the intrinsic sizes, $x_{\rm A,B}^{\rm int}$ by a factor $(1+\epsilon_{\rm A,B}^{\rm A})$ which depends on the orbital period, the pulse period and on

the system geometry[18]. While aberration should eventually become detectable in the timing, allowing the determination of a further PK parameter, at present it leads to an undetermined deviation of x^{obs} from x^{int}, where the latter is the relevant quantity for the mass ratio. The parameter $\epsilon_{\mathrm{A,B}}^{\mathrm{A}}$ scales with pulse period and is therefore expected to be two orders of magnitude smaller for A than for B. However, because of the high precision of the A timing parameters, the derived value $x_{\mathrm{A}}^{\mathrm{obs}}$ may already be significantly affected by aberration. This has (as yet) no consequences for the mass ratio $R = x_{\mathrm{B}}^{\mathrm{obs}}/x_{\mathrm{A}}^{\mathrm{obs}}$, as the uncertainty in R is dominated by the much less precise $x_{\mathrm{B}}^{\mathrm{obs}}$. We can explore the likely aberration corrections to $x_{\mathrm{B}}^{\mathrm{obs}}$ for various possible geometries. Using a range of values given by studies of the double pulsar's emission properties[49], we estimate $\epsilon_{\mathrm{A}}^{\mathrm{A}} \sim 10^{-6}$ and $\epsilon_{\mathrm{B}}^{\mathrm{A}} \sim 10^{-4}$. The contribution of aberration therefore is at least one order of magnitude smaller than our current timing precision. In the future this effect may become important, possibly limiting the usefulness of R for tests of GR. If the geometry cannot be independently determined, we could use the observed deviations of R from the value expected within GR to determine $\epsilon_{\mathrm{B}}^{\mathrm{A}}$ and hence the geometry of B.

In the near and far future, the precision of the all parameters will increase further, because of the available longer time span and also the employment of better instrumentation. In a few years, we should therefore be able to measure additional PK parameters, including those which arise from a relativistic deformation of the pulsar orbit and those which find their origin in aberration effects and their interplay with geodetic precession (see [18]). On secular time scales we will even achieve a precision that will require us to consider post-Newtonian (PN) terms that go beyond the currently used description of the PK parameters. Indeed, the equations for the PK parameters given earlier are only correct to lowest PN order. However, higher-order corrections are expected to become important if timing precision is sufficiently high. While this has not been the case in the past, the double pulsar system may allow measurements of these effects in the future [24].

One such effect involves the GR prediction that, in contrast to Newtonian physics, the neutron stars' spins affect their orbital motion via spin-orbit coupling. This effect would be visible most clearly as a contribution to the observed $\dot{\omega}$ in a secular [40] and periodic fashion [50]. For the J0737−3039 system, the expected contribution is about an order of magnitude larger than for PSR B1913+16, i.e. 2×10^{-4} deg yr^{-1} (for A, assuming a geometry as determined for PSR B1913+16 [43]). As the exact value depends on the pulsars' moment of inertia, a potential measurement of this effect allows the moment of inertia of a neutron star to be determined for the first time [51]. To be successful requires the measurement of at least two other parameters to a similar accuracy as $\dot{\omega}$. While this is a tough challenge, e.g. due to the expected profile variations caused by geodetic precession, the rewards of such a measurement and its impact on the study of the equation of state of neutron stars make it worth trying.

11   Summary & Conclusions

With the measurement of five PK parameters and the unique information about the mass ratio, the PSR J0737−3039 system provides a truly unique test-bed for relativistic theories of gravity. So far, GR also passes this test with flying colours. The precision of this test and the nature of the resulting constraints go beyond what has been possible with other systems in the past. The test achieved so far is, however, only the beginning of a study of relativistic phenomena that can be investigated in great detail in this wonderful cosmic laboratory.

Table 1

Timing parameter	PSR J0737−3039A	PSR J0737−3039B
Right Ascension α	$07^{\mathrm{h}}37^{\mathrm{m}}51^{\mathrm{s}}.24927(3)$	−
Declination δ	$-30°39'40''.7195(5)$	−
Proper motion in the RA direction (mas yr^{-1})	$-3.3(4)$	−
Proper motion in Declination (mas yr^{-1})	$2.6(5)$	−
Parallax, π (mas)	$3(2)$	−
Spin frequency ν (Hz)	$44.054069392744(2)$	$0.36056035506(1)$
Spin frequency derivative $\dot{\nu}$ (s^{-2})	$-3.4156(1) \times 10^{-15}$	$-0.116(1) \times 10^{-15}$
Timing Epoch (MJD)	53156.0	53156.0
Dispersion measure DM (cm^{-3}pc)	$48.920(5)$	−
Orbital period P_b (day)	$0.10225156248(5)$	−
Eccentricity e	$0.0877775(9)$	−
Projected semi-major axis $x = (a/c)\sin i$ (s)	$1.415032(1)$	$1.5161(16)$
Longitude of periastron ω (deg)	$87.0331(8)$	$87.0331 + 180.0$
Epoch of periastron T_0 (MJD)	$53155.9074280(2)$	−
Advance of periastron $\dot{\omega}$ (deg/yr)	$16.89947(68)$	$[16.96(5)]$
Gravitational redshift parameter γ (ms)	$0.3856(26)$	−
Shapiro delay parameter s	$0.99974(-39,+16)$	−
Shapiro delay parameter r (μs)	$6.21(33)$	−
Orbital period derivative $\dot{P_b}$	$-1.252(17) \times 10^{-12}$	−
Timing data span (MJD)	$52760 - 53736$	$52760 - 53736$
RMS timing residual σ (μsec)	54	2169
Total proper motion (mas yr^{-1})	$4.2(4)$	
Distance d(DM) (pc)	~ 500	
Distance $d(\pi)$ (pc)	$200 - 1000$	
Transverse velocity ($d = 500$ pc) (km s^{-1})	$10(1)$	
Orbital inclination angle (deg)	$88.69(-76,+50)$	
Mass function ($M_\odot$)	$0.29096571(87)$	$0.3579(11)$
Mass ratio, R	$1.0714(11)$	
Total system mass ($M_\odot$)	$2.58708(16)$	
Neutron star mass ($m_\odot$)	$1.3381(7)$	$1.2489(7)$

Table 1: Parameters for PSR J0737−3039A (A) and PSR J0737−3039B (B) as measured by Kramer et al. (2006). The values were derived from pulse timing observations using the DD and DDS models of the timing analysis program TEMPO[27] and the Jet Propulsion Laboratory DE405 planetary ephemeris[28]. Estimated uncertainties, given in parentheses after the values, refer to the least significant digit of the tabulated value and are twice the formal 1-σ values given by TEMPO. The positional parameters are in the DE405 reference frame which is close to that of the International Celestial Reference System. Pulsar spin frequencies $\nu \equiv 1/P$ are in barycentric dynamical time (TDB) units at the timing epoch quoted in Modified Julian Days. The five Keplerian binary parameters (P_b, e, ω, T_0, and x) are derived for pulsar A. The first four of these (with an offset of $180°$ added to ω) and the position parameters were assumed when fitting for B's parameters. Five post-Keplerian parameters have now been measured. An independent fit of $\dot{\omega}$ for B yielded a value (shown in square brackets) that is consistent with the much more precise result for A. The value derived for A was adopted in the final analysis. The dispersion-based distance is based on a model for the interstellar electron density[29] and has an uncertainty of order 20%.

Table 2

PK parameter	Observed	GR expectation	Ratio
$\dot{P}_{\mathrm{b}}$	1.252(17)	1.24787(13)	1.003(14)
γ (ms)	0.3856(26)	0.38418(22)	1.0036(68)
s	$0.99974(-39,+16)$	$0.99987(-48,+13)$	0.99987(50)
$r(\mu \mathrm{s})$	6.21(33)	6.153(26)	1.009(55)

Table 2: Four independent tests of GR provided by the double pulsar as presented by Kramer et al. (2006). The second column lists the observed PK parameters obtained by fitting a DDS timing model to the data. The third column lists the values expected from general relativity given the masses determined from the intersection point of the mass ratio R and the periastron advance $\dot{\omega}$. The last column gives the ratio of the observed to expected value for each test. Uncertainties refer to the last quoted digit and were determined using Monte Carlo methods (see Supporting Online Material).

Acknowledgements

References

[1] T. Damour, G. Esposito-Farèse, *Phys. Rev. D* **58**, 1 (1998).

[2] S. E. Thorsett, D. Chakrabarty, *ApJ* **512**, 288 (1999).

[3] J. R. Oppenheimer, G. Volkoff, *Phys. Rev.* **55**, 374 (1939).

[4] V. E. Zavlin, G. G. Pavlov, *A&A* **329**, 583 (1998).

[5] G. F. Bignami, P. A. Caraveo, A. de Luca, S. Mereghetti, *SF2A-2003: Semaine de l'Astrophysique Francaise*, T. C. F. Combes, D. Barret, L. Pagani, eds. (2003), p. 381.

[6] T. H. Hankins, J. S. Kern, J. C. Weatherall, J. A. Eilek, *Nature* **422**, 141 (2003).

[7] M. Blaskiewicz, Ph.D. thesis, Cornell University (1991).

[8] S. Johnston, D. Galloway, *MNRAS* **306**, L50 (1999).

[9] G. Hobbs, A. G. Lyne, M. Kramer, C. E. Martin, C. Jordan, *MNRAS* **353**, 1311 (2004).

[10] W. Zhang, F. E. Marshall, E. V. Gotthelf, J. Middleditch, Q. D. Wang, *ApJ* **554**, L177 (2001).

[11] A. G. Lyne, R. S. Pritchard, F. G. Smith, *MNRAS* **265**, 1003 (1993).

[12] M. Kramer, *et al.*, *ApJ* **593**, L31 (2003).

[13] M. D. Young, R. N. Manchester, S. Johnston, *Nature* **400**, 848 (1999).

[14] D. C. Backer, S. R. Kulkarni, C. Heiles, M. M. Davis, W. M. Goss, *Nature* **300**, 615 (1982).

[15] J. W. T. Hessels, *et al.*, *Science* **311**, 1901 (2006).

[16] M. A. Alpar, A. F. Cheng, M. A. Ruderman, J. Shaham, *Nature* **300**, 728 (1982).

[17] M. Kramer, *et al.*, *Science* **in press** (2006).

[18] T. Damour, J. H. Taylor, *Phys. Rev. D* **45**, 1840 (1992).

[19] T. Damour, N. Deruelle, *Ann. Inst. H. Poincaré (Physique Théorique)* **43**, 107 (1985).

[20] T. Damour, N. Deruelle, *Ann. Inst. H. Poincaré (Physique Théorique)* **44**, 263 (1986).

[21] M. Burgay, *et al.*, *Nature* **426**, 531 (2003).

[22] R. N. Manchester, *et al.*, *MNRAS* **328**, 17 (2001).

[23] V. Kalogera, *et al.*, *ApJ* **601**, L179 (2004).

[24] A. G. Lyne, *et al.*, *Science* **303**, 1153 (2004).

[25] M. A. McLaughlin, *et al.*, *ApJ* **616**, L131 (2004a).

[26] M. A. McLaughlin, *et al.*, *ApJ* **613**, L57 (2004b).

[27] http://www.atnf.csiro.au/research/pulsar/tempo

[28] E. M. Standish, *A&A* **336**, 381 (1998).

[29] J. M. Cordes, T. J. W. Lazio (2002). astro-ph/0207156.

[30] J. M. Weisberg, J. H. Taylor, *Binary Radio Pulsars*, F. Rasio, I. H. Stairs, eds. (Astronomical Society of the Pacific, San Francisco, 2005), pp. 25–31.

[31] I. H. Stairs, S. E. Thorsett, J. H. Taylor, A. Wolszczan, *ApJ* **581**, 501 (2002).

[32] J. H. Taylor, A. Wolszczan, T. Damour, J. M. Weisberg, *Nature* **355**, 132 (1992).

[33] W. A. Coles, M. A. McLaughlin, B. J. Rickett, A. G. Lyne, N. D. R. Bhat, *ApJ* **623**, 392 (2005).

[34] Lorimer, D. R. and Kramer, M., *Handbook of Pulsar Astronomy* (Cambridge University Press, 2005).

[35] M. Kramer, *et al.*, *Annalen der Physik* **15**, 34 (2006).

[36] C. Lange, *et al.*, *MNRAS* **326**, 274 (2001).

[37] S. M. Ransom, *et al.*, *ApJ* **609**, L71 (2004).

[38] J. H. Taylor, *Philos. Trans. Roy. Soc. London A* **341**, 117 (1992).

[39] T. Damour, R. Ruffini, *Academie des Sciences Paris Comptes Rendus Ser. Scie. Math.* **279**, 971 (1974).

[40] B. M. Barker, R. F. O'Connell, *ApJ* **199**, L25 (1975).

[41] M. Burgay, *et al.*, *ApJ* **624**, L113 (2005).

[42] R. N. Manchester, *et al.*, *ApJ* **621**, L49 (2005).

[43] M. Kramer, *ApJ* **509**, 856 (1998).

[44] F. A. Jenet, S. M. Ransom, *Nature* **428**, 919 (2004).

[45] I. H. Stairs, S. E. Thorsett, R. J. Dewey, M. Kramer, C. McPhee, *MNRAS* p. in press (2006).

[46] T. Damour, J. H. Taylor, *ApJ* **366**, 501 (1991).

[47] K. Kuijken, G. Gilmore, *MNRAS* **239**, 571 (1989).

[48] T. Damour, G. Esposito-Far'ese p. Submitted. (2006).

[49] M. Lyutikov, *MNRAS* **362**, 1078 (2005).

[50] N. Wex, *Class. Quantum Grav.* **12**, 983 (1995).

[51] T. Damour, G. Schäfer, *Nuovo Cim.* **101**, 127 (1988).